Pure Appl. Geophys. 173 (2016), 3049–3064

DOI 10.1007/s00024-016-1343-7

Pure and Applied Geophysics

Ice Fog and Light Snow Measurements Using a High-Resolution Camera System

Thomas Kuhn[1] and Ismail Gultepe[2]

Abstract—Ice fog, diamond dust, and light snow usually form over extremely cold weather conditions, and they affect both visibility and Earth's radiative energy budget. Prediction of these hydrometeors using models is difficult because of limited knowledge of the microphysical properties at the small size ranges due to measurement issues. These phenomena need to be better represented in forecast and climate models; therefore, in addition to remote sensing accurate measurements using ground-based instrumentation are required. An imaging instrument, aimed at measuring ice fog and light snow particles, has been built and is presented here. The ice crystal imaging (ICI) probe samples ice particles into a vertical, tapered inlet with an inlet flow rate of 11 L min^{-1}. A laser beam across the vertical air flow containing the ice crystals allows for their detection by a photodetector collecting the scattered light. Detected particles are then imaged with high optical resolution. An illuminating LED flash and image capturing are triggered by the photodetector. In this work, ICI measurements collected during the fog remote sensing and modeling (FRAM) project, which took place during Winter of 2010–2011 in Yellowknife, NWT, Canada, are summarized and challenges related to measuring small ice particles are described. The majority of ice particles during the 2-month-long campaign had sizes between 300 and 800 µm. During ice fog events the size distribution measured had a lower mode diameter of 300 µm compared to the overall campaign average with mode at 500 µm.

Key words: Ice fog, snow, precipitation, fall speed, ice particle properties, optical imaging.

1. Introduction

Ice fog and light snow usually form at cold temperatures below −10 °C when ice nuclei exist in a supersaturated environment with respect to ice. These conditions typically happen at higher latitudes during cold winter conditions such as over Arctic regions. Ice fog and light snow are important weather phenomena as they affect aviation and transportation through visibility reduction (Gultepe et al. 2015b). Forecasting of these weather phenomena, however, is difficult (Gultepe et al. 2009, 2015b), but better knowledge of the microphysical properties of atmospheric ice particles is essential to the development of the meteorological forecast models.

In addition to their role in aviation and transportation safety, these ice particles also influence the radiative transfer in the atmosphere; therefore they affect the Earth's climate significantly (Gultepe et al. 2015a, 2016). Climate modelling studies suggested that ice fog can significantly affect the radiative budget in the Arctic (Girard and Blanchet 2001). Both ice fog and light snow are dominated by smaller ice particles or crystals with sizes below 1 mm. Light scattering by these particles is affected strongly by their shapes (Schlimme et al. 2005) and size distributions. Usually detailed information on particle distributions (as opposed to average or effective sizes) is required for accurate radiative transfer calculations (Mitchell et al. 2011). Thus, measurements of ice crystal shape and size, and their distribution are particularly valuable for assessing climate change issues and for aviation applications.

Parameterizations of ice particle fall speeds were determined for specific ice particles and can be found for example in the work of Locatelli and Hobbs (1974) and Kajikawa and Okuhara (1997). Although improvements of parameterizations based on field and laboratory measurements have been reported (Heymsfield and Westbrook 2010), more direct measurements of terminal velocities for a variety of particle types are needed to develop better parameterizations, so that they can be used to improve climate models and the prediction of mass and heat budget based on numerical forecasting models.

[1] Department of Computer Science, Electrical and Space Engineering, Luleå University of Technology, Kiruna, Sweden. E-mail: thomas.kuhn@ltu.se
[2] Cloud Physics and Severe Weather Research Section, Environment Canada, Toronto, ON, Canada.

Instruments to measure snow ice particles on the ground are limited in their ability to provide detailed microphysical properties such as particle shape and size information. Disdrometers measure the drop or ice crystal size distribution and fall speed of hydrometeors making certain physical assumptions. For example, the particle size velocity, ParSiVel disdrometer (Battaglia et al. 2010) uses the intensity reduction of a horizontal light beam caused by a falling particle to determine particle size distributions and fall speed. Particle shape cannot be retrieved and the lower size limit is usually set at 250 μm. Other disdrometers or optical probes also use one-dimensional optical arrays that provide a two-dimensional shadowgraph of each particle (Gultepe et al. 2015a). The size of the smallest particle that can be detected depends on the pixel resolution (object size corresponding to one pixel of the array). For the optical spectrometer developed by ETH in Zurich the pixel resolution is 150 μm (Barthazy et al. 1998). For the hydrometeor velocity and shape detector (HVSD), horizontal pixel resolution is 0.15 mm and vertical pixel resolution depends on fall speed and is on the same order as the horizontal one for ice particles (Barthazy et al. 2004); and for the two-dimensional video disdrometer (2-DVD) pixel resolution is 200 μm (Kruger and Krajewski 2002). The snowflake video imager (SVI) uses a CCD camera to acquire images at a fixed frame rate and it has a pixel resolution of 50 and 100 μm in the two image directions, respectively (Newman et al. 2009). Another interesting new instrument is the multi-angle snowflake camera (MASC) that captures images from different angles with three higher resolution cameras and measures fall speed (Garrett et al. 2012). The cameras have different resolutions; the finest pixel resolution is 9 μm. However, only snowflakes larger than 100 μm are detected by MASC, and the resolution in falling direction is reduced by the particle's movement to around 40 μm. Hence, all these instruments lack in accurate measurements of particle size and shape for smaller particles. Therefore, such accurate information is also missing for measurements of fall speeds.

Optical array probes that are used on aircraft have smaller pixel resolutions of 25 or 10 μm (Lawson et al. 2006b). Given the low quality and resolution of the shadowgraph images and issues with false multiple particles due to optical breakup (Field et al. 2006; Korolev et al. 1998), measuring size distributions and shape of ice fog particles with these probes are still in question. Aircraft probes with better capability of detecting smaller ice particles are scattering probes that can detect submicrometre particles, such as the forward scattering spectrometer probe (FSSP, Baumgardner et al. 1992), and the cloud particle imager (CPI) probe (Lawson et al. 2001). The former provides particle size distributions without direct shape information. Only indirect and very limited shape information can be retrieved based on shape dependence of light scattering detected in several directions. The latter uses optical imaging with a pixel resolution of 2.3 μm. The CPI has also been used in ground-based experiments. For example, Lawson et al. (2006a) used the CPI at Antarctica with aspirating ice particles at the inlet speed of 30 m s^{-1}, finding that particle size distributions were dominated by particles below 200 μm for light snow fall and diamond dust. Another aircraft probe, the NCAR video ice particle sampler probe VIPS (McFarquhar and Heymsfield 1996), has a relatively good resolution and crystals larger than 5 μm can be detected. The VIPS was used in a ground-based configuration to measure in ice fog conditions in Alaska (Schmitt et al. 2013). In their work the NCAR ice crystal replicator, normally a balloon-borne instrument (Miloshevich and Heymsfield 1997), was also used for ice fog spectral measurements. After collection, the ice crystal replicas were analysed in the laboratory by microscope, thus better resolution is achieved compared to the VIPS or CPI. In their Alaska field study, Schmitt et al. (2013) found that for temperatures colder than −30 °C, most particles are below 30 μm in size with concentrations generally increasing from very low values at 100 μm to a maximum at about 10 μm. Gultepe et al. (2014) used GCIP, a ground-based version of the aircraft CIP optical array probe (Baumgardner et al. 2001) for ice fog studies. The shape measurements of ice crystals from GCIP were limited by its poorer resolution (pixel resolution of 15 μm) showing the need for a better probe to detect size, shape, and size distributions of ice crystals.

The overall goals of this work are to contribute to a better characterization of ice fog particle microphysical properties as well as small snow crystal properties for modelling and observational studies. Observations, representing ice fog and light snow crystals, were carried out during the FRAM project (fog remote sensing and modeling), which took place over Yellowknife International Airport, NWT, Canada during winter of 2010–2011 (Gultepe et al. 2014, 2015b), and are used in achieving the goals. For accomplishing this work, the following objectives are considered: (1) present a ground-based instrument, called the ice crystal imaging (ICI) probe that provides size, shape, and fall speed of small ice particles; (2) show the capability of ice crystal fall-speed (V_f) measurement using ICI probe; (3) derive microphysical characteristics of small ice crystals applicable to cloud-climate studies; and (4) compare the results with other studies to validate accuracy of present measurements.

2. Field Project and Observations

A field campaign dedicated to ice fog studies called the fog remote sensing and modeling-ice fog (FRAM-IF) field project took place near the Yellowknife International Airport (62°27′46″N, 114°26′25″W), Yellowknife, NWT, Canada, from 25 November 2010 to 5 February 2011. Details of the FRAM project observations, the project site, and the instruments employed during the campaign can be found in Gultepe et al. (2014, 2015b). The main observations collected during the project were related to ice crystal size spectra and shape, aerosol spectra, visibility (Vis), temperature (T), relative humidity (RH), precipitation rate and amount (PR and PA), and 3D wind components. The ice crystal imaging (ICI) probe was installed on a pole approximately 1 m above the roof of a trailer used during the project.

During the campaign, ice fog events usually occurred related to cold high-pressure systems with clear skies and cold temperatures down to about −30 °C, which is colder than those of average weather conditions. Several ice fog, diamond dust, and often light snow conditions were observed, and these are summarized in Gultepe et al. (2014).

3. Methods

In this section, the ICI instrument set-up and image analysis technique to determine ice fog and light snow microphysical characteristics are described.

3.1. Instrument Set-up

The ICI probe acquires optical images of small ice and snow crystals. It has been used for the first time at the FRAM-IF project and has been described by Gultepe et al. (2014). Here, its important features related to ice fog and snow crystals' size and shape are described. The optical camera system for imaging the ice particles [shown in Gultepe et al. (2014) and in Fig. 1] is similar to the microscope optics, using a bright-field imaging set-up, described by Kuhn et al. (2012). Here, the magnification has been adapted based on the expected particle sizes, resulting in a pixel resolution of 4.22 μm. Illumination for particle imaging is provided by intense LED light flashes.

The ICI probe has a vertical funnel-shaped inlet that has an upward facing opening of 25 mm in diameter. Ice crystal and snow particles that are smaller than about 100 μm are sampled efficiently at the 11-L min^{-1} inlet flow rate as they follow the air stream into the inlet given their low Stokes numbers (0.4 at 100 μm and lower for smaller sizes). Larger ice particles (having larger Stokes numbers) are not following the sample flow into the inlet effectively; however, they settle into the inlet opening at their own fall speed. To guide this passive collecting method of ice crystals the inlet flow rate of 11 L min^{-1} and inlet opening of 25 mm have been chosen so that the mean air speed across the inlet opening, about 0.4 m s^{-1}, is within the range of typical fall speeds. In this way the sample volume determined from the inlet flow rate (see Sect. 3.2) is characteristic for both particles below and above 100 μm; however, particles settling at larger speeds will be overestimated. After entering the inlet, particles are transferred, using the principles of a virtual impactor (Gultepe et al. 2014), to a vertical tube with 12 mm inner diameter. The sampling efficiency of this virtual impactor step can be derived from the Stokes number of the flow through its nozzle and is for ICI 50 % at approximately 9 μm, and it rises quickly with

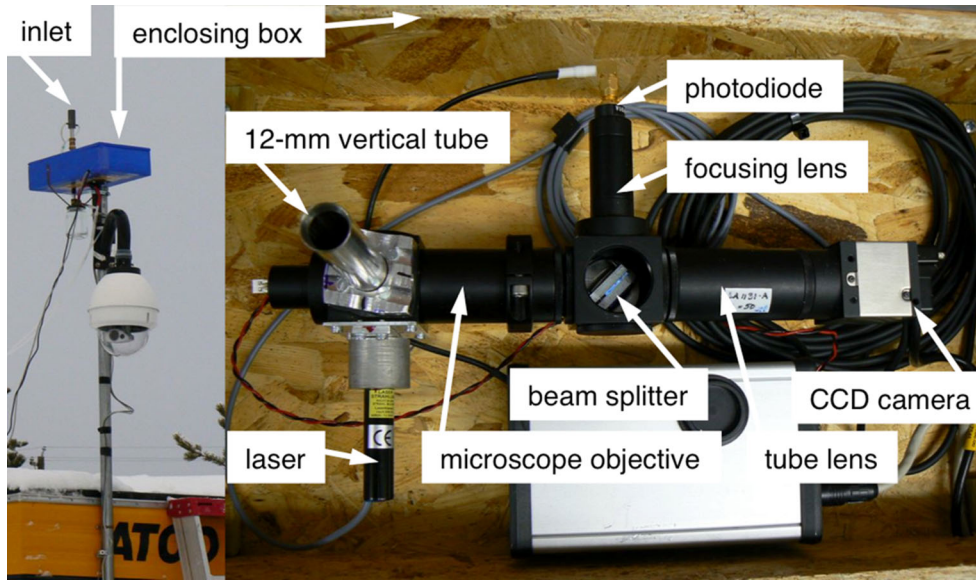

Figure 1
The ICI probe at the FRAM-IF measurement campaign. On the *left*: the probe installed at the campaign site (on a pole on top of the campaign container), inlet and enclosing box can be seen. On the *right*: the probe inside the enclosing box seen from above (inlet and box cover removed). The components that are explained in the text are labelled on the figure

increasing size to around 90 % at 10 μm according to numerical solutions presented by Rader and Marple (1985). Four lateral glass windows in this 12-mm vertical tube allow for detecting and imaging of ice crystals. Two windows are used for imaging and illumination of ice crystals, respectively. They are arranged at opposite sides of the tube wall, along the optical axis defined by the imaging system consisting of microscope objective, tube lens, and CCD camera. The optical axis is perpendicular to the vertical tube axis. The two additional windows are placed along a laser beam, which is perpendicular to both those axes. The laser light enters and leaves through these windows. Particles traversing this laser beam in the centre of the tube are detected by the scattered light intensity that is collected at 90° angle to the laser beam. The scattered light is collected by the same optics that is used for imaging, i.e. the microscope objective, and is then directed onto a photodiode detector through a beam splitter. Thereby, the sensing volume is defined by the intersection of the laser beam with the field of view (FOV) of the imaging optics. After ice crystal detection, image acquisition is triggered and the ice crystal's image is saved for further processing in image analysis.

3.2. *Image Analysis*

Ice crystal size and projected area are determined using automatic image analysis code as described in Kuhn et al. (2012). Figure 2 shows examples of typical ice crystal images. The maximum dimension D is defined as the diameter of the smallest circle that completely encloses the particle on the image and it is used to describe the characteristic size of the analysed particles. The ice crystal sizes and areas are then used in obtaining microphysical properties, such as particle size distributions (PSD) and area ratio (Ar, a shape descriptor defined in Sect. 4.2), that are used for developing physical parameterizations for possible use in numerical forecast models.

The number concentration of ice crystals is obtained using the particle count and the corresponding sampling volume that requires an accurate flow rate parameter. All ice crystals entering the inlet are transferred to the 12-mm vertical tube. Then, a certain fraction of these ice crystals traverses the probe's sensing volume, within the 12-mm tube, where they are detected and imaged for future processing. Hence, the effective sample flow rate used in the calculations is defined as the fraction of

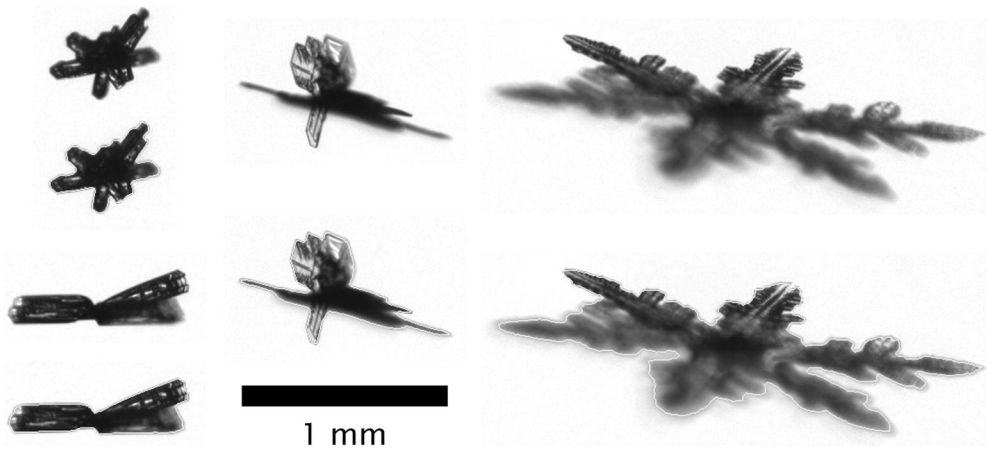

Figure 2
Examples of ice particle images. The particle boundary found by image analysis is shown in a *second image* underneath each particle image as well. The *black bar* for size comparison has a length of 1 mm and height of 100 μm

the inlet flow rate of 11 L min^{-1} that contains the detected ice crystals. This fraction is obtained from the sensing area (the cross-sectional area of the sensing volume as seen from above along the direction of flow) divided by the cross section of the 12-mm tube. The sensing area is given by the product of the width of the FOV (4.32 mm) and the sensing depth where particles are detected, which is the sum of the laser beam depth (approximately 0.5 mm) and the size of the particles. This accounts for the fact that an ice particle is detected by the laser beam even if the laser only partially hits the particle. For simplicity, it is assumed that the depth of the sensing area is 1 mm, which is the effective sensing area corresponding to a 500-μm particle size. Then, the sensing area becomes 4.32 mm^2, resulting in a sample flow rate of 7.0 mL s^{-1}. This simplification results in underestimating number concentration of smaller particles and overestimating number concentration of larger particles.

The size range, in which particles are measured, has a lower limit given by the detection through scattered light. Particles smaller than this lower size limit do not scatter enough light to be detected. The used set-up with 90° scattering allows for a simple optical set-up; however, it also has a relatively high lower size limit of around 100 μm. While it is desirable and possible to modify the set-up to allow for detecting smaller particles, this modification was not done during this study. The upper limit of the size range is given by the FOV of 4.32 mm × 3.24 mm and the vertical position of the laser beam. The laser, which is used for detecting particles and triggering the imaging, influences directly the location of particles on the images. The laser beam is located in the centre and focused vertically to a thin sheet. Hence, particles larger than approximately half the height of the FOV cannot be imaged completely. In fact, almost no particle larger than 1.5 mm is imaged without touching the upper border of the image. Particles touching any border of the image are rejected from analysis, as their size becomes uncertain. This results in an upper size limit for particles being measured of around 1.5 mm. The random horizontal location of particles yields a probability of particles touching the right or left image border, which increases with increasing particles size. This results in underestimating the number concentration of larger particles, but it is compensated by the overestimation of larger particles due to the simplification of using a constant, size-independent sampling volume. An effective correction factor for number concentration that would account for both effects would indeed be close to one for ice particle sizes between 1 and 1.5 mm. Below 1 mm this correction factor, which has not been considered in this first data analysis, increases slowly while particle size decreases, and finally reaches approximately 1.3 at 500 μm and 1.7 at 100 μm.

3.3. Set-up for Determining Fall Speed

During the campaign, the instrument was operated for 7 days in a modified set-up mode that allowed to determine the ice crystal fall speed in addition to measurements of ice crystal size, projected area, and shape. The modified set-up did not provide active sample flow rate, and the inlet as well as the 12-mm tube were removed for obtaining accurate fall speeds. The optical cell is larger in this set-up and particles are allowed to fall freely into it, so that their fall speed will not be modified. Detected particles are then captured twice on the same image by illuminating the particle with two flashes instead of one. Time difference between the two illuminating flashes was 1.64 ms. Using the vertical displacement of a particle on the image, V_f is calculated. Automatic image analysis was difficult due to particles appearing twice on the same image, and sometimes, these two particle appearances were overlapping. Therefore, the outline of the particle area was traced by hand and the vertical displacement was determined during the analysis. Then, the fall speed, size, and area were retrieved from subsequent automatic analysis.

4. Results and Discussion

The ICI has been operated at its first campaign, FRAM-IF, over almost 60 days between 30 November 2010 and 30 January 2011. During this time, ice particles have been measured at temperatures between −5 and −37 °C. Gultepe et al. (2014) suggested that ice fog occurrence was more than 20 % of time during the project. Light snowfall was also measured at 30 % of the time. During the project, snow or ice particles were detected during 343 1-h periods. In general, total ice crystal number concentrations (N_t) were low; more than half of this time N_t was less than 0.2 L^{-1}. The average N_t during the whole period was approximately 0.6 L^{-1}. The maximum hourly average N_t during the campaign was 8 L^{-1}. All detected particles have been considered for these number concentrations. For the rest of the analysis, particles that touch the border of an image or appear to be fragmented are excluded. The latter issue results from out-of-focus particles, leading to sizing uncertainties. Thus, 35 % of particles, because of these issues, were excluded from analysis. The remaining particles were detected during 304 1-h periods. As was to be expected, most of the excluded particles were relatively large, with an average measured size of 1.3 mm, whereas the remaining particles with a mean size of 660 μm were un-fragmented and did not touch the border.

4.1. Ice Particle Size Distributions

Particle size distributions (PSDs), or size spectra, of snow and ice particles are determined using the ice crystal number concentrations N_i counted at each of the size bins, which are spaced at 100 μm intervals. The PSD of all ice particles for the whole campaign, given by N_i of all size bins normalized with the bin width is shown in Fig. 3. This PSD represents the average of snow or ice N_i detected during all 1-h periods when particles were detected, i.e. the average over 304 h. The corresponding N_t was obtained as 0.45 L^{-1}, and ice crystal sizes ranged from 20 μm to 3.5 mm. In addition, PSDs for two shorter events, representing ice fog and light snow conditions are also shown in Fig. 3, scaled for better comparison. The actual N_t for the ice fog and snow events are 0.11 and 0.95 L^{-1}, respectively.

The PSD of ice and snow crystals for the entire campaign had a mean particle size D of 660 μm with one mode between 300 and 800 μm. During the ice fog event on 16 and 17 January 2011, ice crystal sizes are distinctly shifted towards smaller sizes, with mean $D = 550$ μm. However, one needs to consider that the sharp decline in N_i below around 200 μm is in part caused by the lower size limit of around 100 μm. If this lower limit were decreased, the size distribution would likely shift even further towards smaller sizes, as is to be expected by comparison to the aforementioned ice fog study by Schmitt et al. (2013) with maxima in the PSDs at approximately 10 μm. However, the PSDs during that study in Alaska were observed at colder temperatures than in this study. During the light snowfall event on December 7 2010, larger sizes of ice crystals were detected, with mean $D = 730$ μm, i.e. larger than both for the campaign average and the ice fog event. For this snow PSD, which shows the largest sizes, N_i

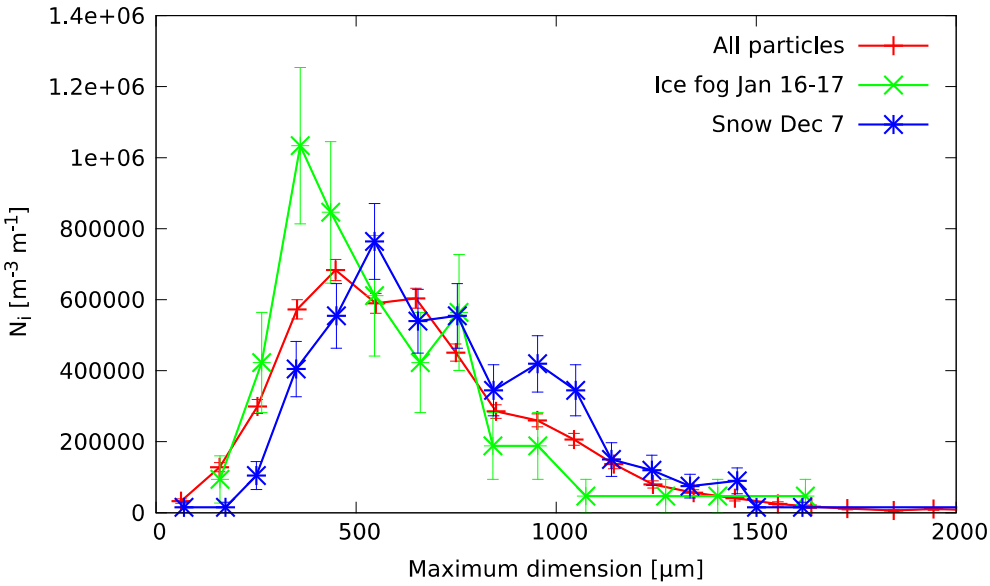

Figure 3
The PSD of all particles is shown (as *red curve*). For each size bin, N_i is normalized by the bin width, and is shown at the mean size of particles in that bin. This PSD represents the average during all 304 1-h periods when snow or ice particles were detected. The total number concentration of the PSD is 0.45 L^{-1}. PSDs for two shorter events, ice fog and light snow, are also shown. They are scaled for better comparison. The total number concentrations N_t for the ice fog and snow events are 0.11 and 0.95 L^{-1}, respectively

becomes almost zero before the sizes increase to the upper size limit of 1.5 mm.

4.2. Ice Crystal Area Dependency on Size

The projected areas of all analysed particles for the entire FRAM-IF campaign are plotted against crystal maximum dimensions D in Fig. 4. The cross-sectional areas of spherical particles are also shown for comparison. An area–dimensional relationship given by the power law as $A = \alpha \times D^{\beta}$ provides a good fit to observations obtained as

$$A = 1.99 \times 10^{-12} \times D^{1.72}, \qquad (1)$$

where correlation coefficient R^2 is 0.88, and A and D are in units of m^2 and µm, respectively. The shorter episodes of ice fog and snowfall had a higher R^2 and also a steeper slope parameter (higher β). For ice fog, the parameters were $\beta = 1.94$, $\alpha = 5.55 \times 10^{-13}$, and $R^2 = 0.95$. For snowfall, $\beta = 1.74$, $\alpha = 1.99 \times 10^{-12}$, and $R^2 = 0.92$. The better correlation is likely related to natural variability, which for shorter episodes is less than for the campaign-long averages because it represents various weather events. Three area–dimensional power law relationships for stellar and broad-branched ice crystals obtained from Pruppacher and Klett (1978) and for bullet rosettes from Mitchell (1996) are also shown in Fig. 4. These relationships also represent our observational data reasonably well and differences can be addressed based on variability of ice crystal properties within the different thermodynamical conditions.

Particles with areas well below the majority of data at similar sizes appear as outliers on the area-versus-size plot (Fig. 4). Most of these particles were observed at temperatures above −22 °C where ice crystals in clouds grow predominantly to larger plates and stellar crystals by diffusional processes. Closer examination of the images reveals that many of these particles were stellar and plate-like (seen from the side) with relatively small areas compared to the majority of particles at similar sizes D. A few examples of these ice crystal images are shown in Fig. 5.

The projected areas of ice crystals are also analysed using the area ratio defined as

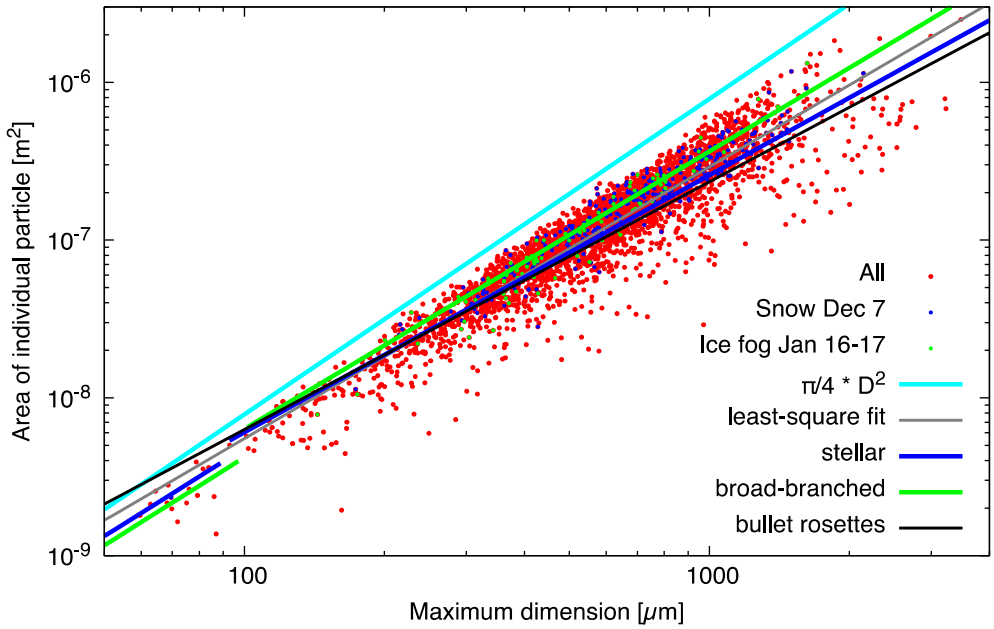

Figure 4
Measured area of individual particles plotted versus size D (maximum dimension). Particles from an ice fog and a light snowfall event are marked using *different colours*. For comparison, the areas of circles with diameter equal to maximum dimension are shown as well as area–dimensional power law relationships for stellar and broad-branched ice crystals from Pruppacher and Klett (1978) and for bullet rosettes from Mitchell (1996)

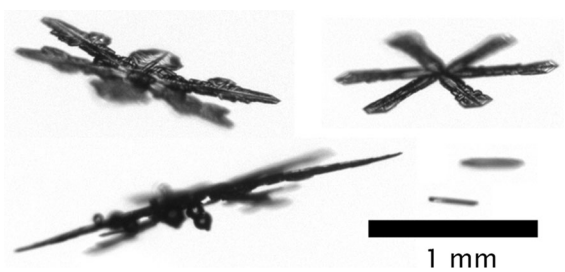

Figure 5
Example images of ice crystals with, for their size, relatively small areas and area ratios Ar. From *top left clockwise*, Ar and temperature of the particles are: 0.16, −16 °C; 0.16, −14 °C; 0.11, −13 °C; 0.17, −13 °C; and 0.064, −13 °C. The *black bar* for size comparison has a length of 1 mm and height of 100 μm

$$\mathrm{Ar} = \frac{A}{\frac{\pi}{4}D^2}, \tag{2}$$

where the measured area A is divided by the cross-sectional area of a spherical particle with diameter given by the particle's maximum dimension D. Figure 6 shows Ar versus D for ice crystals during the whole campaign. The observations for temperatures above and below −22 °C are shown with red and green coloured points, respectively. In Fig. 6, area ratios averaged over size bins of 100 μm width are also shown. Results show systematically smaller Ar for ice crystals at higher temperature, which include the above-mentioned 'outliers' in Fig. 4. A few example particles of these outliers are shown in Fig. 5; the relatively small areas A, compared to the majority of particles at similar maximum dimensions D, result in relatively small Ar values. For the ice particles shown in Fig. 5 Ar varied between 0.06 and 0.17, and they were observed at temperatures of about −14 °C.

4.3. Mass and Effective Diameter

Mass–dimensional relationships are commonly used for estimating ice crystal mass directly from their size. Similarly to the spread of measured particle areas for any given D, ice crystal masses likely also cover a wide range of values. However, a mass–dimensional relationship, representing averaged

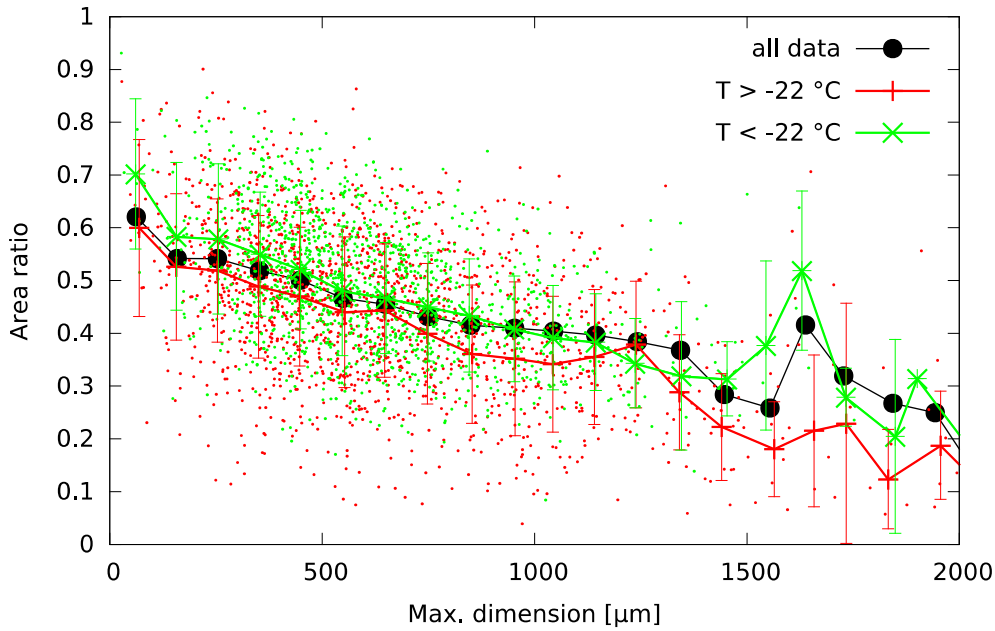

Figure 6
Area ratios (Ar) of individual particles versus maximum dimension (*D*). Particles with relatively small area (*A*) have relatively small Ar. The data in *different colours* represent temperatures above and below −22 °C, respectively. The *points connected by lines* show Ar averaged within each size bin; the overall average, as well as averages for above and below −22 °C are also shown. *Error bars* indicate standard deviation of Ar in the respective size bins

conditions, would yield only one mass for any given *D*. Therefore, an ice particle area-to-mass relationship can be used to obtain a more realistic ice crystal mass. Baker and Lawson (2006) showed with measurements of snow particles collected on the ground (Mitchell et al. 1990) that ice crystal mass can be determined more accurately from the area of an ice particle rather than from its size. For that reason, their mass–area relationship is used here as

$$m = 0.115 \times 10^{-6} \times A^{1.218}, \qquad (3)$$

where m and A are the mass and area in units of kg and mm^2, respectively, of single ice particles.

Figure 7 shows ice crystal mass m versus size D. The relationship by Baker and Lawson (2006) is overestimated, with respect to mass of spherical particles, below about 100 µm, a size range where they did not measure ice particles. Because only a few particles are affected form this overestimation in our study, we have not used a different relationship for these small particles with sizes less than 100 µm. Since the ICI probe did not measure mass directly, we have to rely on a mass–size or mass–area relationships obtained from the literature. The variability in mass that can result from using different relationships, including three mass–dimensional power laws for stellar and broad-branched ice crystals (Pruppacher and Klett 1978) and for bullet rosettes (Mitchell 1996) can be seen in Fig. 7. These relationships resulted in up to approximately five times less mass compared to the estimates obtained from Baker and Lawson (2006). Mass could also be estimated by assuming a certain effective thickness (mass is then given by area times thickness). Examining images captured by ICI showed that the smallest thickness of plate-like features of ice particles during the campaign was on the order of approximately 25–30 µm. Thus, by assuming a thickness of 25 µm for the ice crystals, an estimate of mass that represents the lower limit of mass for any given particle is obtained as

$$m = 25\,\mu\text{m} \times \rho_{\text{ice}} \times A, \qquad (4)$$

where the density of ice ρ_{ice} is assumed as 917 kg m^{-3}. This lower limit estimate results in masses similar to those obtained by the two

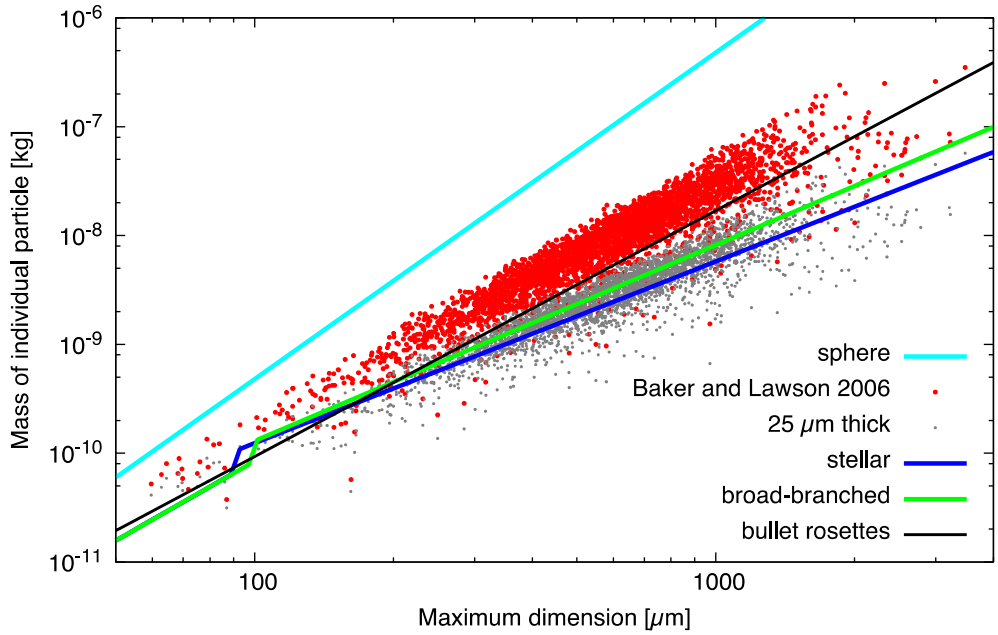

Figure 7
Mass of individual particles plotted versus size (maximum dimension, D). The masses of ice spheres with diameter D are indicated in the *figure* for comparison. The mass is estimated from the measured areas of ice particles using the mass–area relationship from Baker and Lawson (2006). A second estimate is shown for assumed constant thickness of 25 μm, representing a lower limit for mass when particles are thin and plate-like. The mass–D power law relationships for stellar and broad-branched ice crystals from Pruppacher and Klett (1978) and for bullet rosettes from Mitchell (1996) are also shown for comparison. Of these, the two relationships for plate-like particles from Pruppacher and Klett (1978) are close to the lower limit estimate

relationships for plate-like particles from Pruppacher and Klett (1978) (Fig. 7).

Using Eq. (3) to estimate mass from ice crystal projected area, each PSD from Fig. 3 is converted to a mass distribution (Fig. 8). The total mass concentration (defined as ice water content, IWC) for the three size distributions in this figure is obtained as 6.7 $\times$ 10^{-3} g m^{-3}, 1.4 $\times$ 10^{-3} g m^{-3}, and 18 $\times$ 10^{-3} g m^{-3} for the entire campaign average, the ice fog event, and the light snow event, respectively. PSDs corresponding to mass estimated by assuming an effective thickness of 25 μm (Eq. 4) are also shown (as grey lines) in Fig. 8. These results are found to be similar but with much lower values, and these resulted in IWC of 1.8 $\times$ 10^{-3} g m^{-3}, 0.38 $\times$ 10^{-3} g m^{-3}, and 4.6 $\times$ 10^{-3} g m^{-3} for the entire campaign average, the ice fog event, and the light snow event, respectively.

The effective diameter (D_{eff}), defined as the ratio of particle ensemble volume to area, can be calculated using the ice crystal volumes (or masses) and areas. While area is measured directly, mass is determined from a mass–size or mass–area relationship. In general, D_{eff} increases with increasing mean D. This can be seen in Fig. 9 that shows D_{eff} values for 1-h periods, which were calculated using the definition of D_{eff} from Foot (1988) given as

$$D_{\text{eff}} = \frac{3m_{\text{c}}}{2\rho_{\text{ice}}A_{\text{c}}}, \tag{5}$$

where ρ_{ice} is the density of ice and m_{c} and A_{c} are the mass and projected area concentrations, respectively, of the ice crystal ensembles under consideration. The ratio of m_{c} to A_{c} is equal to the ratio of average (during the 1-h periods) single particle mass to area, and these are calculated from single particle measured areas A and estimated masses m as determined from the mass–area relationship of Baker and Lawson (2006) given by Eq. (3). The majority of the 1-h mean D values is below 1000 μm where D_{eff} is between 30 and 150 μm (Fig. 9). The D_{eff} of the three PSDs shown in both Figs. 3 and 8 is approximately

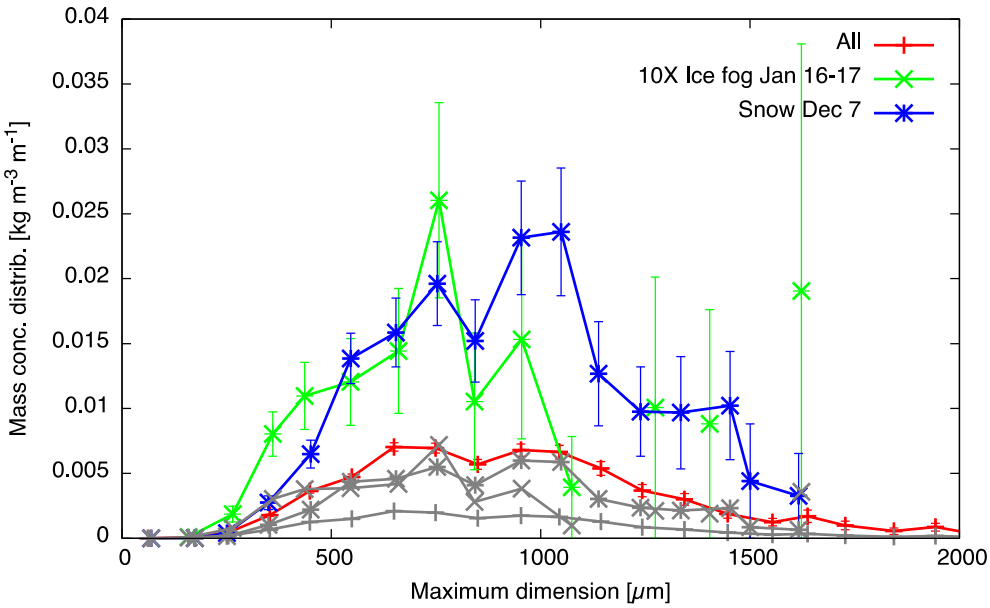

Figure 8
As in Fig. 3, but here the mass size distributions are shown instead of PSDs. Mass of individual particles was estimated using the mass–area relationship from Baker and Lawson (2006) to determine mass concentrations in the size bins. The ice water content (IWC) for the three distributions shown are 6.7×10^{-3} g m^{-3} for the campaign average, and 1.4×10^{-3} g m^{-3} and 18×10^{-3} g m^{-3} for the ice fog and light snow events, respectively. The distribution for ice fog is scaled by a factor of 10 for better visualization. The three PSDs shown in grey (using the same *point symbols* to indicate the same cases, and with the same scaling for ice fog case) use a constant thickness of 25 μm to estimate mass (*see text*) and represent a lower limit in mass uncertainty

141, 139, and 143 μm, for the entire campaign average, the ice fog event, and the light snow event, respectively. The uncertainty in mass calculation discussed above due to the particular choice of mass relationship translates also directly to uncertainty in D_{eff}, which is proportional to mass (Eq. 5). Hence, the selection of a mass relationship among the many parameterizations from literature strongly influences the resulting D_{eff}. This can be seen in Fig. 9, which shows D_{eff} obtained for the three mass–dimensional relationships for stellar and broad-branched ice crystals from Pruppacher and Klett (1978) and for bullet rosettes from Mitchell (1996) using the corresponding area–dimensional relationships. Also shown is the constant D_{eff} value obtained from the ice crystal mass using a crystal thickness of 25 μm. As expected, D_{eff} from the two relationships for plate-like particles from Pruppacher and Klett (1978) is close to this constant value. The uncertainty in D_{eff} is size-dependent, lower for conditions with on average smaller particles and larger for conditions with predominantly larger particles.

4.4. Fall Speed Versus Size and Area

The fall speed of ice crystals was measured during 7 days of the campaign. The instrument set-up was modified during December 7–14 to allow for obtaining V_{f} measurements (see Sect. 3.3). Some examples of the images acquired while measuring the fall speed are shown in Fig. 10.

Figure 11 shows V_{f} versus D (upper panel) and versus A (lower panel) for three ice crystal habits. Ice crystals on Dec 7 at about −20 °C were usually found to be crystals of type sideplane, plate-like and stellar, or bullet rosette. The fall speed V_{f} as a function of D and A does not show a clear trend but with increasing size and area, the spread in V_{f} decreases, possibly due to drag of large surface areas of ice crystals. The smaller the area, the larger the variability of V_{f}. This suggests that drag is affected by orientation and density of ice crystals so that these likely played an important role for V_{f}. Ice crystals having shapes such as sideplanes and plates do not show a clear trend. For bullet rosettes, on the other

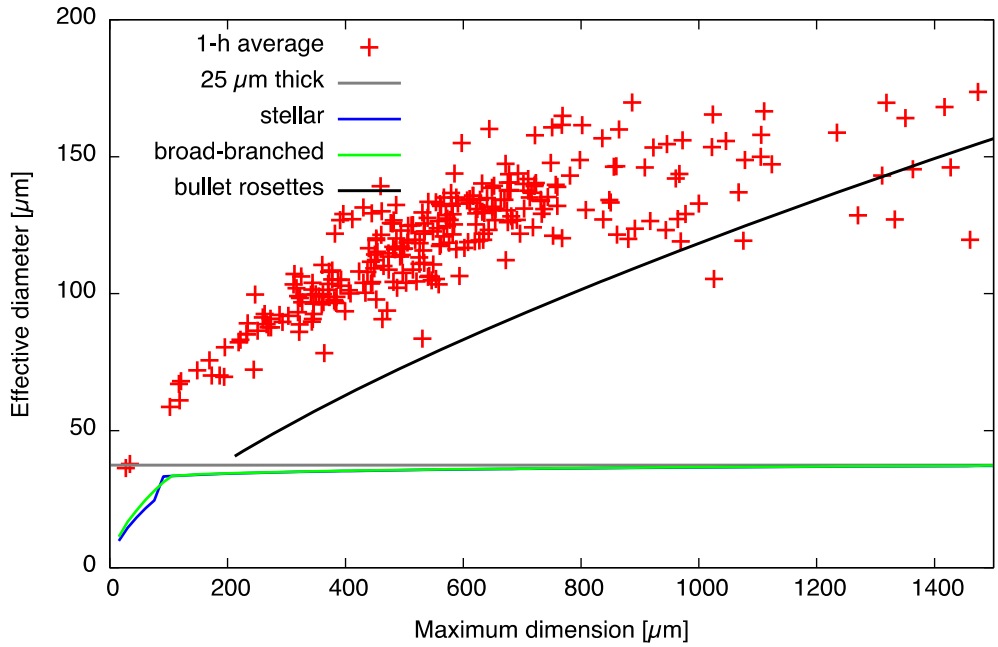

Figure 9
Effective diameter D_{eff} (Foot 1988) computed for 1-h periods is shown as a function of the average maximum dimension. The D_{eff} for the mass–dimensional relationships for stellar and broad-branched ice crystals from Pruppacher and Klett (1978) and for bullet rosettes from Mitchell (1996) are also shown. For consistency, the corresponding area–dimensional relationships, instead of measured area, are used, resulting in curves for D_{eff} instead of scattered points. Also shown is the constant D_{eff} resulting from the mass determined using a thickness of 25 μm

hand, a clear dependence of V_{f} on size and area is seen. This can likely be due to the drag being largely independent from orientation for this shape class.

The wind speed measured was generally low (below about 3 m s^{-1}) and did not vary significantly during the fall-speed measurements. This suggests that wind speed or near-surface turbulence did not affect the measured fall speed. This was confirmed by dividing the data set in two groups corresponding to wind speed below and above the median value, respectively. Fall speed versus D and versus A did not reveal significant differences between the two groups (not shown). While this demonstrates the ability of ICI with modified inlet to measure fall speed, more data are needed to verify fall-speed measurements and analyse them more in detail.

5. Conclusions

In this work, ice crystal and light snow characteristics are studied using ICI probe with an integrated camera system. Its observations were performed during the FRAM-IF project, which took place in Yellowknife, NWT, Canada, during winter of 2010–2011.

The main conclusions of this work can be presented as follows:

- The specially developed ICI probe can be used to determine microphysical characteristics of small ice crystals with sizes less than about 1500 μm. When properties such as ice crystal size, shape, and fall speed are determined for these small ice crystals, new relationships for numerical model applications can be derived.
- The size range considered here includes ice crystal sizes less than 500 μm, which are more important than large ice crystals for the radiative effect and heat budget due to the large number of these small ice crystals (Gultepe et al. 2014, 2015b).
- The ICI probe can measure size, projected area, shape of single ice crystals, fall speeds, total number concentration, and provides PSD. The

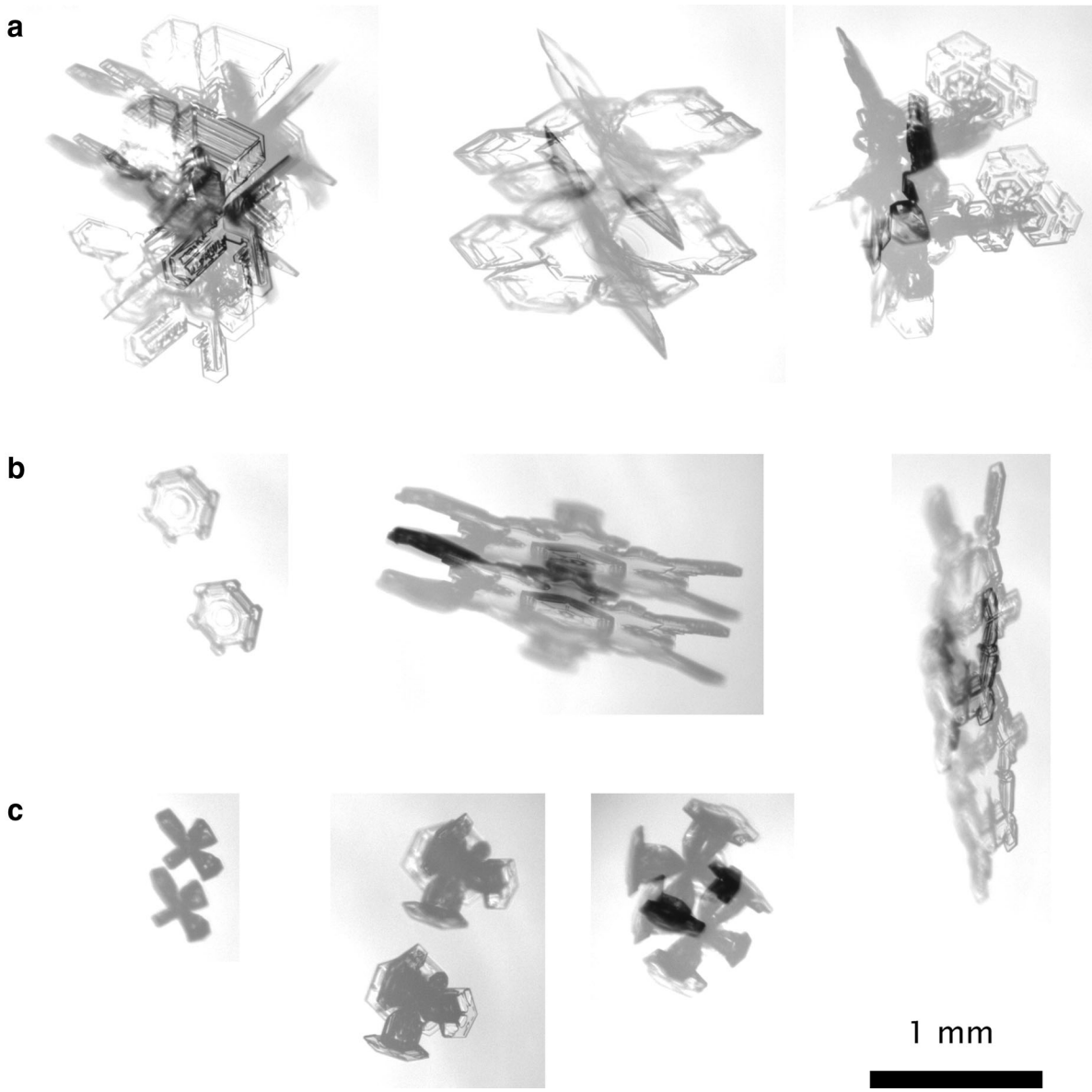

Figure 10
Example images acquired while testing a set-up for measuring fall speed. The falling ice particles are captured twice on the same images by illuminating with two flashes instead of one. The vertical displacement divided by the 1.64-ms temporal separation yields fall speed. **a** Examples of falling particles of type sideplane; **b** plate-like and stellar type; **c** bullet rosettes type. The *black bar* for size comparison has a length of 1 mm and height of 100 μm

high-resolution images from the probe add valuable details on the small ice crystals and their effect on microphysical parameterizations.

- The measured projected areas of ice crystals versus D during the whole campaign were approximated by the power law of $A = 1.99 \times 10^{-12} \times D^{1.72}$. Despite the large spread of data points, which represents the natural variability, a good correlation was found with $R^2 = 0.88$. Correlation coefficients were larger for the shorter events because of lower variability of predominant shapes and atmospheric conditions.

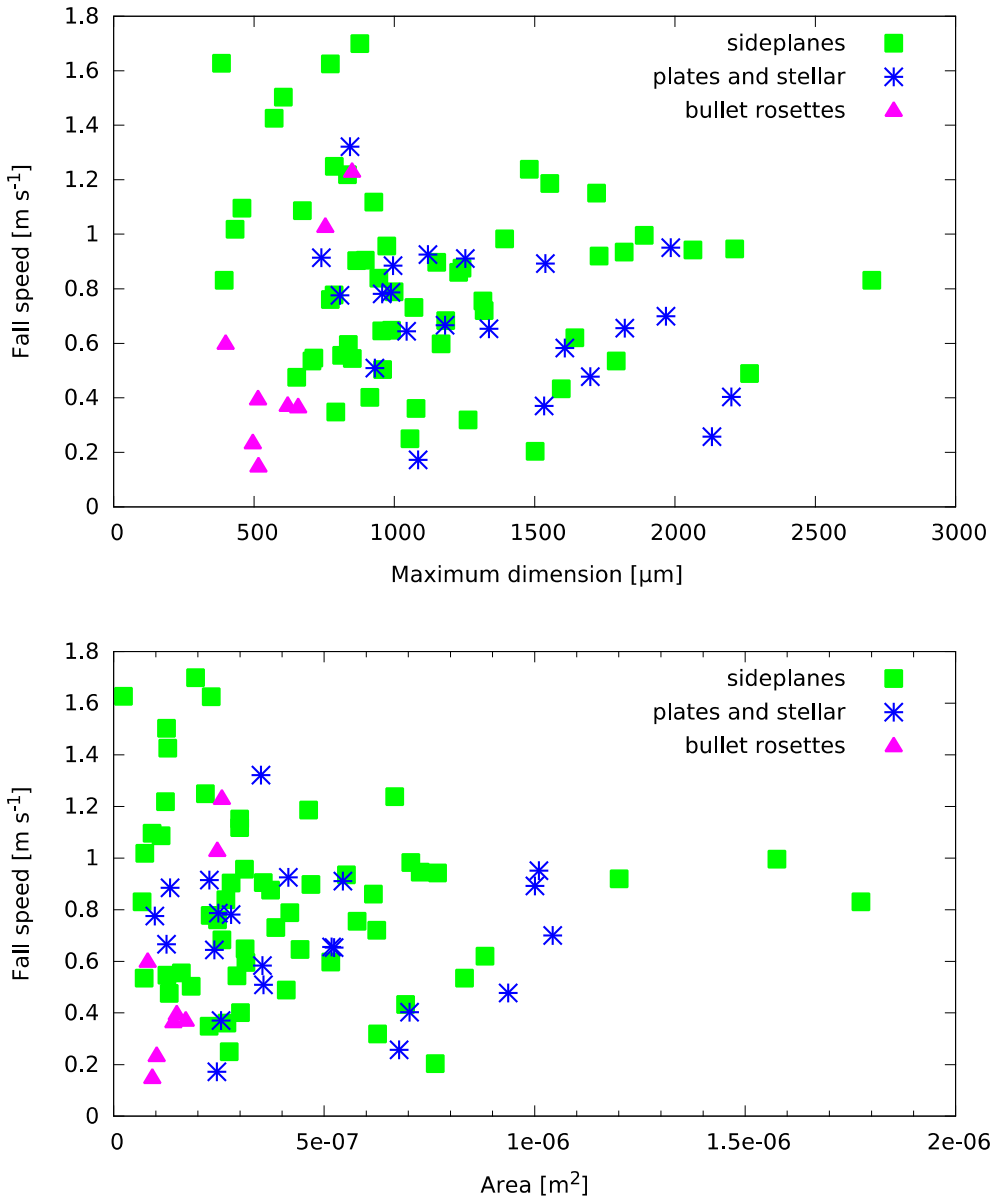

Figure 11
Fall speed versus maximum dimension (*upper panel*) and area (*lower panel*), respectively. The *plots* show fall speeds from ice particles on a day with temperatures around −20 °C, and particle shapes mostly of types sideplane, plate-like and stellar, or bullet rosette. Large variations likely stem from dependence on ice crystal orientation (for plate-like and stellar type) and their complex shapes (sideplane type)

- It was shown that a modification of ICI is well suited to measure fall speed of ice and snow crystals with sizes less than about 1500 µm. The image quality of ice crystals can allow better analysis of particle orientation effects on V_f. In addition, ice crystals can easily be sorted for different shape classes to develop better V_f and IWC parameterizations.
- The lower size limit of the ICI probe during the campaign was approximately 100 µm and upper size limit around 1.5 mm. The upper limit did not present a problem in this study because ice

fog and snow particles were much smaller than 1 mm at cold temperatures. The strength of the instrument is to provide detailed information on these small ice crystals with high-resolution optical images. However, the instrument could also be modified to allow larger particles to be measured.

- With respect to the lower size limit, it is foreseen that future measurements after lowering the size threshold for particle detection below 100 μm would improve the capabilities of measuring ice fog and small crystal properties.

Overall, it is concluded that ICI probe measurements, compared to other optical sensors available, can improve the numerical model prediction of ice crystal microphysical parameters, visibility, and climate modelling through heat budget estimations. Therefore, its use for future Arctic applications, specifically for ice fog and light snow conditions (Gultepe et al. 2015a) would improve heat and moisture budgets of cold climates and our understanding of ice clouds.

Acknowledgments

We like to thank Swedish National Space Board, National Search and Rescue Secretariat (SAR) of Canada, and Environment Canada for funding this work.

References

Baker, B., & Lawson, R. (2006). Improvement in determination of ice water content from two-dimensional particle imagery. Part I: Image-to-mass relationships. *Journal of Applied Meteorology and Climatology, 45*(9), 1282–1290.

Barthazy, E., Göke, S., Schefold, R., & Högl, D. (2004). An optical array instrument for shape and fall velocity measurements of hydrometeors. *Journal of Atmospheric and Oceanic Technology, 21*(9), 1400–1416.

Barthazy, E., Henrich, W., & Waldvogel, A. (1998). Size distribution of hydrometeors through the melting layer. *Atmospheric Research, 47–48*(SI), 193–208.

Battaglia, A., Rustemeier, E., Tokay, A., Blahak, U., & Simmer, C. (2010). PARSIVEL snow observations: A critical assessment. *Journal of Atmospheric and Oceanic Technology, 27*(2), 333–344. doi:10.1175/2009JTECHA1332.1.

Baumgardner, D., Dye, J. E., Gandrud, B. W., & Knollenberg, R. G. (1992). Interpretation of measurements made by the forward scattering spectrometer probe (FSSP-300) during the airborne Arctic stratospheric expedition. *Journal of Geophysical Research Atmospheres, 97*(D8), 8035–8046.

Baumgardner, D., Jonsson, H., Dawson, W., O'Connor, D., & Newton, R. (2001). The cloud, aerosol and precipitation spectrometer: A new instrument for cloud investigations. *Atmospheric Research, 59–60*, 251–264. doi:10.1016/S0169-8095(01)00119-3.

Field, P., Heymsfield, A., & Bansemer, A. (2006). Shattering and particle interarrival times measured by optical array probes in ice clouds. *Journal of Atmospheric and Oceanic Technology, 23*(10), 1357–1371.

Foot, J. S. (1988). Some observations of the optical-properties of clouds: 2. Cirrus. *Quarterly Journal of the Royal Meteorological Society, 114*(479), 145–164. doi:10.1002/qj.49711447908.

Garrett, T. J., Fallgatter, C., Shkurko, K., & Howlett, D. (2012). Fall speed measurement and high-resolution multi-angle photography of hydrometeors in free fall. *Atmospheric Measurement Techniques, 5*(11), 2625–2633. doi:10.5194/amt-5-2625-2012.

Girard, E., & Blanchet, J.-P. (2001). Microphysical parameterization of Arctic diamond dust, ice fog, and thin stratus for climate models. *Journal of the Atmospheric Sciences, 58*(10), 1181–1198. doi:10.1175/1520-0469(2001)058<1181:MPOADD>2.0.CO;2.

Gultepe, I., et al. (2016). An overview of MATERHORN mountain ice fog project: Observations and predictability. *Pure and Applied Geophysics* **(accepted for publication)**.

Gultepe, I., Hansen, B., Cober, S. G., Pearson, G., Milbrandt, J. A., Platnick, S., et al. (2009). The fog remote sensing and modeling field project. *Bulletin of the American Meteorological Society, 90*, 341–359. doi:10.1175/2008BAMS2354.1.

Gultepe, I., et al. (2014). Ice fog in Arctic during FRAM-Ice Fog project: Aviation and nowcasting applications. *Bulletin of the American Meteorological Society, 95*, 211–226. doi:10.1175/BAMS-D-11-00071.1.

Gultepe, I., Rabin, R., Ware, R., & Pavolonis, M. (2015a). Light snow measurements over cold climatic regions. *Advances in Geophysics* **(submitted)**.

Gultepe, I., et al. (2015b). A review on ice fog: Measurements and modeling. *Atmospheric Research, 151*(SI), 2–19.

Heymsfield, A. J., & Westbrook, C. D. (2010). Advances in the estimation of ice particle fall speeds using laboratory and field measurements. *Journal of the Atmospheric Sciences, 67*, 2469–2482. doi:10.1175/2010JAS3379.1.

Kajikawa, M., & Okuhara, K. (1997). Observations of the falling motion of plate-like snow crystals. 2. The free-fall patterns and velocity variations of rimed crystals. *Journal of the Meteorological Society of Japan, 75*(4), 811–818.

Korolev, A., Strapp, J., & Isaac, G. (1998). Evaluation of the accuracy of PMS optical array probes. *Journal of Atmospheric and Oceanic Technology, 15*(3), 708–720.

Kruger, A., & Krajewski, W. F. (2002). Two-dimensional video disdrometer: A brief description. *Journal of Atmospheric and*

Oceanic Technology, 19, 602–617. doi:10.1175/1520-0426(2002)019<0602:TDVDAD>2.0.CO;2.

Kuhn, T., Grishin, I., & Sloan, J. J. (2012). Improved imaging and image analysis system for application to measurement of small ice crystals. *Journal of Atmospheric and Oceanic Technology, 29*, 1811–1824. doi:10.1175/JTECH-D-11-00199.1.

Lawson, R. P., Baker, B. A., Schmitt, C. G., & Jensen, T. L. (2001). An overview of microphysical properties of Arctic clouds observed in May and July 1998 during FIRE ACE. *Journal Geophysical Research, 106*(D14), 14989–15014.

Lawson, R. P., Baker, B. A., Zmarzly, P., O'Connor, D., Mo, Q., Gayet, J. -F., & Shcherbakov, V. (2006a). Microphysical and optical properties of atmospheric ice crystals at South Pole station. *Journal of Applied Meteorology and Climatology, 45*(11), 1505–1524. doi:10.1175/JAM2421.1.

Lawson, R., O'Connor, D., Zmarzly, P., Weaver, K., Baker, B., Mo, Q., & Jonsson, H. (2006b). The 2D-S (Stereo) probe: Design and preliminary tests of a new airborne, high-speed, high-resolution particle Imaging probe. *Journal of Atmospheric and Oceanic Technology, 23*(11), 1462–1477.

Locatelli, J. D., & Hobbs, P. V. (1974). Fall speeds and masses of solid precipitation particles. *Journal Geophysical Research, 79*, 2185–2197.

McFarquhar, G. M., & Heymsfield, A. J. (1996). Microphysical characteristics of three anvils sampled during the Central Equatorial Pacific Experiment. *Journal of the Atmospheric Sciences, 53*(17), 2401–2423.

Miloshevich, L. M., & Heymsfield, A. J. (1997). A balloon-borne continuous cloud particle replicator for measuring vertical profiles of cloud microphysical properties: Instrument design, performance, and collection efficiency analysis. *Journal of Atmospheric and Oceanic Technology, 14*(4), 753–768.

Mitchell, D. L. (1996). Use of mass and area dimensional power laws for determining precipitation particle terminal velocities. *Journal of the Atmospheric Sciences, 53*(12), 1710–1723.

Mitchell, D. L., Lawson, R. P., & Baker, B. (2011). Understanding effective diameter and its application to terrestrial radiation in ice clouds. *Atmospheric Chemistry and Physics,*. doi:10.5194/acp-11-3417-2011.

Mitchell, D. L., Zhang, R., & Pitter, R. L. (1990). Mass-dimensional relationships for ice particles and the influence of riming on snowfall rates. *Journal of Applied Meteorology, 29*, 153–163.

Newman, A. J., Kucera, P. A., & Bliven, L. F. (2009). Presenting the snowflake video imager (SVI). *Journal of Atmospheric and Oceanic Technology, 26*(2), 167–179. doi:10.1175/2008JTECHA1148.1.

Pruppacher, H. R., & Klett, J. D. (1978). *Microphysics of clouds and precipitation* (p. 714). Boston: D. Reidel.

Rader, D. J., & Marple, V. A. (1985). Effect of ultra-Stokesian drag and particle interception on impaction characteristics. *Journal of the Atmospheric Sciences, 4*(2), 141–156. doi:10.1080/02786828508959044.

Schlimme, I., Macke, A., & Reichardt, J. (2005). The impact of ice crystal shapes, size distributions, and spatial structures of cirrus clouds on solar radiative fluxes. *Journal of the Atmospheric Sciences, 62*, 2274–2283.

Schmitt, C. G., Stuefer, M., Heymsfield, A. J., & Kim, C. K. (2013). The microphysical properties of ice fog measured in urban environments of Interior Alaska. *Journal Geophysical Research, 118*(19), 11136–11147. doi:10.1002/jgrd.50822.

(Received October 25, 2015, revised June 15, 2016, accepted June 24, 2016, Published online July 11, 2016)